RSC Advances

Volume 1 | Number 1 | Jan 2013 | Pages 1–100

RSC Advances

www.rsc.org/advances

ROYAL SOCIETY OF CHEMISTRY

This is an *Accepted Manuscript*, which has been through the Royal Society of Chemistry peer review process and has been accepted for publication.

Accepted Manuscripts are published online shortly after acceptance, before technical editing, formatting and proof reading. Using this free service, authors can make their results available to the community, in citable form, before we publish the edited article. This *Accepted Manuscript* will be replaced by the edited, formatted and paginated article as soon as this is available.

You can find more information about *Accepted Manuscripts* in the **Information for Authors**.

Please note that technical editing may introduce minor changes to the text and/or graphics, which may alter content. The journal's standard **Terms & Conditions** and the **Ethical guidelines** still apply. In no event shall the Royal Society of Chemistry be held responsible for any errors or omissions in this *Accepted Manuscript* or any consequences arising from the use of any information it contains.

ROYAL SOCIETY OF CHEMISTRY

www.rsc.org/advances

Journal Name

ARTICLE

Ag sensitized TiO₂ and NiFe₂O₄ three-component nanoheterostructures: synthesis, electronic structure and strongly enhanced visible light photocatalytic activity

Andris Šutka,*[a,b] Tanel Käämbre,[a] Rainer Pärna,[a] Nicola Döbelin,[c] Martins Vanags,[d] Krisjanis Smits,[d] Vambola Kisand [b]

This study reports on the synthesis and characterisation of two- and three-component visible light active photocatalytic nanoparticle heterostructures, based on TiO₂ and NiFe₂O₄ and sensitized with Ag. We observe that Ag content as small as 1 at.% in the TiO₂/NiFe₂O₄ heterostructure increases by more than an order of magnitude the rate constant for the visible light photocatalytic process. We rationalise this in terms of the measured structure and electronic structure data of the binary and ternary combinations of the component materials and focus on details, which show that an optimised deposition sequence is vital for attaining the high values of photocatalytic efficiency, because the charge transfer across the interfaces appears to be sensitive to where the Ag is loaded in the heterostructure. The overall higher visible light photocatalytic activity of the TiO₂/Ag/NiFe₂O₄ heterostructure was observed and is attributed to enhanced charge carrier separation efficiency and migration via vectorial electron transfer.

Introduction

Regardless of the large number of research works related to photocatalysts, a search for alternative efficient and cost effective visible-light-active photocatalytic materials of limited ecological footprint remains highly relevant. TiO₂ is very commonly used as a photocatalyst to destroy pollutants due to its relatively high efficiency, high chemical stability, low toxicity and appropriate flat-band potential.[1] Still, the recombination rate of photo-generated electron-hole pairs on TiO₂ is rather high,[2] and the band gap (3.2 eV) is too wide to utilise visible light.[3] Apart from doping with for example transition metal cations in order to introduce impurity states in the band gap of anatase and thereby visible absorption, one way to address these limitations is by combining TiO₂ with narrow band-gap semiconductors and/or noble metals to form two- or three-component all-solid-state heterostructures,[4-9] which apart from the obvious benefit of introducing visible light absorption also can achieve much reduced recombination rates by means of charge separation across the interfaces.[6,10] For that to be efficient, the component materials should be chosen such that growth at interfaces enables intimated contact and the (conduction and valence) band edge potential differences of

the component materials favour the photogenerated charge cross-border migration away from the region of most intense photoexcited electron-hole pair generation. A number of systems have been proposed where the three component heterostructures couple two semiconductors and a noble metal in an all-solid state Z-scheme[6,11,12] or hybrid plasmonic heterostructures with vectorial photogenerated charge separation.[13-15] Overall, noble metal plasmonic sensitizers in photocatalytic heterostructures have demonstrated excellent visible light harvesting properties and effective promotion of photogenerated charge separation/transfer.[14] From among the known existing plasmonic sensitizers, Ag is more readily available due to the lower price and its higher terrestrial abundancy in comparison with Pt, Au or Pd. Additionally, Ag has high conductivity and electron-storing capacity.[15] There are also several studies where all three components of such nano-heterostructured systems are semiconducting oxides.[16-19] As an example, a recent study of mixed anatase/vanadium oxide nanowires reported a several times increased sunlight photocatalytic efficiency when sensitised with silver oxide.[18] As a general trend, three component nanoheterostructures tend to outperform the two component systems, not least due to the improved versatility of photogenerated charge carrier separation.

In the present study, we investigate how coupling anatase TiO₂ to nickel ferrite (NiFe₂O₄) and/or to Ag will improve the overall visible light photocatalytic efficiency. Given the (plasmonic)

a. Institute of Physics, University of Tartu, Ravila 14c, 50411 Tartu, Estonia. E-mail: andris.sutka@ut.ee
b. Institute of Silicate Materials, Riga Technical University, Paula Valdena 3/7, Riga LV-1048, Latvia.
c. RMS Foundation, Bischmattstrasse 12, 2544 Bettlach, Switzerland
d. Institute of Solid State Physics, University of Latvia, Kengaraga 8, 1063 Riga, Latvia

broad spectrum visible absorption of silver nanoparticles and the relatively narrow band gap of NiFe$_2$O$_4$, as well as the band alignment at the interfaces of the heterostructures,[8,20,21] such composition was anticipated to be a good candidate for improved visible light photocatalytic performance. NiFe$_2$O$_4$ has a 1.56 eV indirect band gap,[22,23] and its conduction band minimum (CBM) potential (–1.62 VSCE on the electrochemical scale at pH = 7)[24] is more negative than that of TiO$_2$ (–0.5 VSCE)[1,25] (the corresponding CBM positions relative to the Fermi edge in these materials are 0.2 eV[1] for anatase and 1.44 eV[25] for the ferrite; the latter can be compared to a more moderate value of 0.75 eV for vanadium oxide used in a similar system as mentioned above[18]), which results in a sizeable potential gradient that favours the photoexcited electrons in the ferrite to cross the interface. The spinel type compounds such as NiFe$_2$O$_4$ are also known for their excellent chemical and photo-corrosion stability.[24] From a different aspect, NiFe$_2$O$_4$ is also ferrimagnetic due to the uncompensated spins of nickel cations located at the octahedral sites of the inverse spinel structure,[26] which becomes relevant in allowing the use of magnetic traps to recover the used photocatalyst from waste water. The Ag sensitized three component (TiO$_2$-Ag)/NiFe$_2$O$_4$ heterostructure (with the silver photodeposition on the 25 nm anatase nanoparticles as the initial and the ferrite co-precipitation as the terminal synthesis step), where the silver appears (as shown below) to take the form of 1-2 nm size metallic nanoparticles, was seen to have superior photocatalytic activity over the binary heterostructures, but also over the alternative ternary heterostructure where the silver was photodeposited in a terminal step after the co-precipitation of the ferrite on the anatase (we speculate this to be the result of the presence of active adsorption sites on both TiO$_2$ and NiFe$_2$O$_4$). In order to gain more detailed insight into the processes related to each constituent and interface, pristine constituents as well as samples containing their binary combinations (TiO$_2$/Ag, TiO$_2$/NiFe$_2$O$_4$) were measured for comparison

alongside the three component heterostructures both as regards visible light photocatalytic efficiency and the electronic structure, which are to be related to the details of the relatively straightforward and cost-effective synthesis sequences.Experimental

2.1. Materials

Anatase TiO$_2$ nanoparticles (size <25nm, 99.7%), silver nitrate (AgNO$_3$, 99%), nickel nitrate hexahydrate (Ni(NO$_3$)$_2$·6H$_2$O, >99%), iron(III) nitrate nonahydrate (Fe(NO$_3$)$_3$·9H$_2$O, ≥98%), sodium hydroxide (NaOH, ≥98%), oxalic acid (C$_2$H$_2$O$_4$, 98%) and methylene orange (MO) were purchased from Sigma-Aldrich. All solutions were prepared with Milli-Q water.

2.2. Sample synthesis

To obtain the TiO2-Ag (TA) sample, Ag was deposited on the anatase nanoparticles using a standard Ag photodeposition method.[27] The powder material to be Ag-coated was dispersed at a 1 g/l concentration into an aqueous solution of AgNO$_3$ (2×10^{-4} M). In the next step the pH of the solution was adjusted to 2.0 by adding 0.1 M of an aqueous oxalic acid solution. The solution was stirred and irradiated with UV-vis light using a metal halide lamp (GTV MH400) for 1 h and then left in the dark for 5 h, after which the powder was filtered and washed with Milli-Q water several times, dried at 60°C overnight and annealed at 150 °C for 3 h. Finally, the initial white colour of the commercial TiO$_2$ anatase nanopowder changed into a greyish purple/brown for the TA sample.

To obtain the NiFe$_2$O$_4$ nanoparticles, 0.2 M Ni(NO$_3$)$_2$·6H$_2$O and 0.4 M Fe(NO$_3$)$_3$·9H$_2$O aqueous solutions were mixed at a volume ratio of 1:1, and a 5 M NaOH aqueous solution was added dropwise until reaching pH=12. The mixture was then heated to 80 °C and stirred for 3 h in a capped glass vial. The precipitates obtained after the stirring were washed with Milli-Q water and dried at 60 °C for 24 h. The binary TiO$_2$/NiFe$_2$O$_4$ (sample TN) and the ternary (TiO$_2$-Ag)/NiFe$_2$O$_4$ (sample TAN) were obtained similarly, but after mixing together 25 ml of the 0.2 M Ni(NO$_3$)$_2$·6H$_2$O and 25 ml of the 0.4 M Fe(NO$_3$)$_3$·9H$_2$O aqueous solutions, 1.5 g of commercial TiO$_2$ anatase (for sample TN) or the Ag loaded TiO$_2$ anatase (for sample TAN) nanopowder was dispersed by ultrasonification in the obtained solution, prior to the dropwise addition of the 5 M NaOH solution until reaching pH=12. The TiO$_2$/NiFe$_2$O$_4$ theoretical weight ratio 75/25 was found to be optimal in our previous study.[21] The alternatively ordered (TiO$_2$/NiFe$_2$O$_4$)/Ag (TNA) ternary sample was obtained by subjecting a portion of the previously obtained binary TN sample to the Ag photodeposition sequence. Finally, all the samples were annealed at 150°C for 3 h.

2.3. Sample characterisation

The synthesised powders were analysed by powder X-ray diffraction (XRD) to determine the crystalline phases present.

ARTICLE

A CubiX[3] diffractometer (PANalytical, Almelo, The Netherlands) equipped with a CuKα X-ray tube and a graphite monochromator in the secondary beam was used to acquire datasets in a 2θ range from 10 to 90° with a step size of 0.015° and a counting time of 1 second per step. The crystalline phases were identified by comparing peak positions with the PDF-4+ database (ICDD 2012) and quantified with Rietveld refinement using the BGMN version 4.2.22 software. Crystal structure templates for all identified phases were also adopted from the PDF-4+ database: TiO_2 (anatase, PDF# 04-007-0701), Ag (PDF# 04-001-2617), $NiFe_2O_4$ (PDF# 04-014-8286), Fe_2O_3 (hematite, PDF# 04-003-2900), FeO(OH) (goethite, PDF# 04-015-2989), and Ag_2O (PDF# 04-004-5271). During the refinement it was observed that the fluorescence radiation of Fe ions in CuKα radiation was effectively eliminated by the secondary beam monochromator. For major phases, the scale factor, unit cell dimensions, anisotropic peak broadening, and texture were refined. For minor phases, peak broadening was refined isotropically and texture was not refined. The diffraction pattern of $NiFe_2O_4$ exhibited excessive peak broadening due to the nanometre-sized crystallite sizes. The crystallite size was therefore only refined from the pure $NiFe_2O_4$ sample. The obtained value for crystallite size was used for all other samples containing $NiFe_2O_4$ as a fixed input value.

To measure the light absorbance of nanopowder samples, a Shimadzu UV-Visible spectrophotometer, UV-3700 (Shimadzu Scientific Instruments Kyoto, Japan) with barium sulphate-coated integrating sphere ISR-240A (wavelength range from 240 to 800 nm). A Kubelka–Munk conversion was applied to a diffuse reflectance spectrum to compensate for differences in raw diffuse reflectance spectra from its transmission equivalent.[28]

Scanning electron microscopy (SEM) and elemental mapping images were recorded using a FEI FIB-SEM Helios NanoLab 600 instrument equipped with an Oxford INCA 350 EDX system fitted with an X-Max 50 mm SDD-type detector.

The crystallite size and morphology studies were performed using a transmission electron microscope (TEM, Tecnai G20, FEI) operated at 200 kV. For better seperation of different particles, both direct (TEM) and scanning (STEM) modes were used. Sample elemental analysis EDX (EDAX) for verification of selected particles was done in the STEM mode. The samples for TEM were mixed with ethanol and an ultrasonic bath was used for powder treatment. The obtained solutions for TEM/STEM studies were placed on a holey carbon film on 400 mesh copper grid (Agar Scientific S147-4).

Specific surface areas S (m^2/g) for synthesized samples were calculated by Brunauer–Emmett–Teller (BET) method. Nitrogen adsorption–desorption isotherms were recorded by using instrument NOVA 1200e; Quantachrome, UK.

The X-ray absorption (XAS) and photoelectron spectroscopy (XPS) experiments were carried out at the D1011 beamline at the MAX-II storage ring of the MAX-Lab synchrotron radiation facility (Lund, Sweden). The beamline is equipped with a modified SX-700 plane grating monochromator. The monochromator resolution was better

than 0.2 eV at the O 1s, 0.3 eV at the Fe 2p and 0.4 eV at the Ni 2p absorption threshold. The spot size at the sample was approximately 0.5 mm. The XAS data were measured in total electron yield mode by recording the sample photocurrent. The XPS spectra were measured by an electron energy analyser SCIENTA SES-200 in a fixed analyser transmission (FAT) mode with 200 eV pass energy. The sample powders were pressed into indium foil and were positioned at a normal emission towards the photoelectron spectrometer, with 40° incident angle for the incoming photon beam. The binding energy scales for XPS experiments were referenced to the binding energies of the In 3d5/2 (444.6 eV)[29] and C 1s (adventitious carbon at 284.8 eV) peaks in the spectra of the samples, and the Au 4f lines from a sputter cleaned gold foil reference sample. Although such calibration is adequate for most purposes, the possible small energy drifts (primarily of the excitation energy) that can be present at the beamline did not completely resolve the doubts related to determining the Ag oxidation state. Therefore additional care was taken to ascertain credible distinction between the sub-linewidth binding energy differences of the Ag 3d peak positions of metallic (at 368.1 eV binding energy) and oxidised (367.7 eV) silver in the Ag 3d spectra, in which case the relevant nanostructured samples, an Ar$^+$ sputter cleaned silver foil and a Ag_2O reference were re-measured at home lab using a Scienta SES100 spectrometer with non-monochromatised Al-Kα excitation.

2.4. Determination of photocatalytic activity

Photocatalytic activities were evaluated through the degradation of MO dye in an aqueous solution under visible light irradiation, using a 100 W light-emitting diode (LED) light source (emission band approximately 415-700 nm). MO is a widely used model dye for photocatalytic experiments, thus allowing comparison of experimental results between different studies of the efficiencies of various photocatalytic agents. The initial concentration of MO in the reaction vessel was fixed at 10 mg/l with a photocatalyst loading of 1 g/l. The rate of the MO dye degradation was monitored after certain time intervals by taking 1.4 ml of the samples from each set, centrifuging and analysing using a spectrophotometer. Photocatalytic activities of the synthesized samples were estimated quantitatively by employing the pseudo-first order reaction and calculating the rate constant (k) of MO degradation. The kinetic equation for the pseudo-first order reaction can be written as $\ln(C_0/C)=kt$, where C_0 is the initial concentration of the MO in solution and C is the MO concentration after degradation for a period of time (t).[4,30]
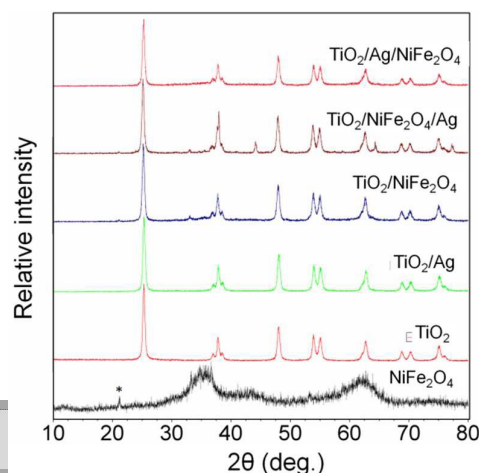
Results and discussion

Fig. 1 XRD patterns of the synthesised samples (a): co-precipitated $NiFe_2O_4$, commercial anatase TiO_2, $TiO_2/NiFe_2O_4$, TiO_2-Ag, (TiO_2-Ag)/$NiFe_2O_4$. Closer view of the co-precipitated $NiFe_2O_4$ XRD pattern (b) with the FeOOH (101) reflex marked by an asterisk.

The XRD data of the samples is displayed in Figure 1. The anatase TiO_2 nanoparticles are seen to be free from polymorphs or contaminations, and to have a crystallite size of 32.1 ± 0.6 nm (isotropic Rietveld refinement). The as-synthesised $NiFe_2O_4$ sample did not allow phase quantification due to the nano-crystalline nature of the phase leading to excessive peak broadening (as also observed elsewhere for similar samples)[31]. The mean $NiFe_2O_4$ crystallite size obtained from Rietveld refinement was 1.73 ± 0.03 nm. This result was used as a fixed input value for all other samples containing $NiFe_2O_4$. In the $TiO_2/NiFe_2O_4$ sample the major components were the two admixed phases TiO_2 (anatase) and $NiFe_2O_4$, although small amounts (less than 2 wt.%) of Fe_2O_3 (hematite)
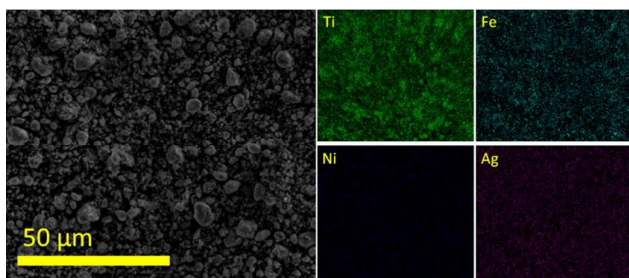
and FeO(OH) (goethite) appeared to be present. The XRD pattern of the TiO_2-Ag (TA) sample was only seen to contain the reflexes of the anatase crystalline phase, whereas the TiO_2-Ag/$NiFe_2O_4$ (TAN) pattern appeared to additionally contain the broad features of the nano-crystalline $NiFe_2O_4$.

Fig. 2 SEM images of commercial anatase TiO_2, co-precipitated $NiFe_2O_4$, TiO_2-Ag, $TiO_2/NiFe_2O_4$, TiO_2-Ag/$NiFe_2O_4$ and $TiO_2/NiFe_2O_4$/Ag heterostructures.

Compared to both the TAN and the TN samples, the TNA sample contained relatively less $NiFe_2O_4$, which could be partly dissolved during Ag photodeposition at low pH. The XRD peaks corresponding either to metallic Ag or to oxidised silver (Ag_2O) were not detected in either of the silver-containing samples TA or TAN, which is somewhat unexpected even in view of the estimated low concentration of silver in the former samples, because metallic Ag exhibits strong XRD pattern even at relatively low amounts (below 1 % wt) due to the high symmetry, crystallinity, and scattering intensity of the structure. However, as seen below from the TEM, EDX, XPS and optical absorption measurements, the silver is definitely present, and we take the absence of sharp Ag reflexes here as an indication of peak broadening due to Ag remaining in the sample in the form of 1-2 nm size nanoparticles, as seen below in TEM images.

The microstructure of the samples was visualised using SEM. SEM micrographs of the different samples are shown in Figure 2. Commercial anatase TiO_2 powder consists of nanoparticles with a size less than 30 nm, while during co-precipitation $NiFe_2O_4$ nanoparticles are formed which are smaller than 10 nm with narrow size distribution (the smaller crystallite size as deduced from the XRD data above indicates that the particles on average consist of more than one crystallite). One of the reasons for the formation of the ultrafine spinel ferrite nanoparticles in chemical co-precipitation is the low process temperature of 80 °C. From SEM images of the different heterostructures it can be seen that they exhibit some differences in microstructure in comparison with non-modified TiO_2.
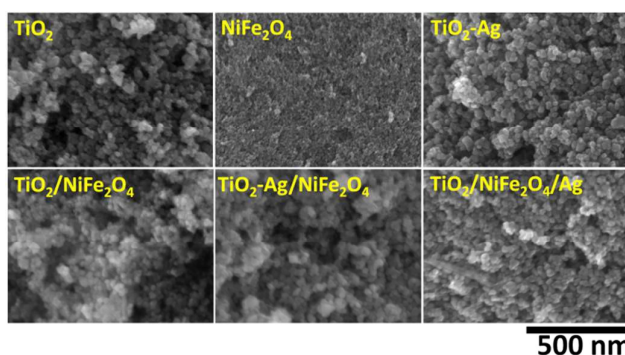

Fig. 3 SEM image and elemental mapping images for TiO_2-Ag/$NiFe_2O_4$ sample.

The SEM elemental map of the TAN sample in Figure 3 shows that on average all elements are dispersed homogeneously in the sample powder with no obvious segregated phases. The EDX spectra (signal averaged over the image area) indicated that the Ag had been successfully loaded onto the TiO_2 sample, and that the relative amount of Ag on the TiO_2 after photodeposition is about 0.7 at.%, which is at least at the level reported previously for deposition under similar conditions.[27]
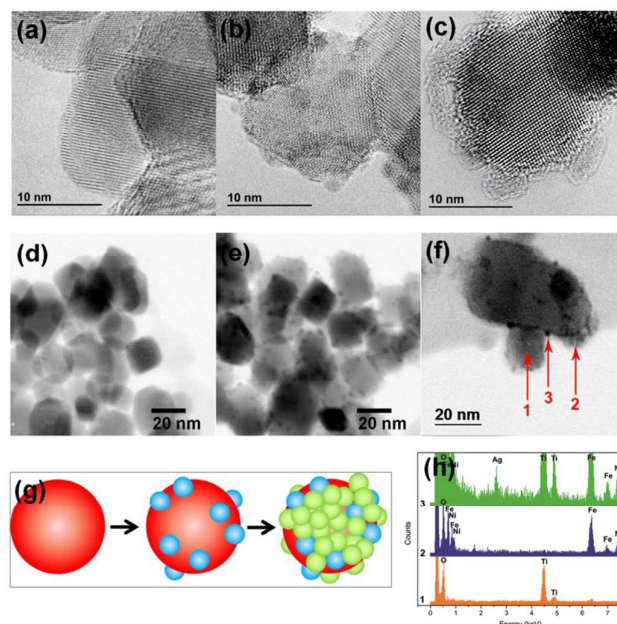
RSC Advances

Journal Name

ARTICLE

Fig. 4 TEM images of (a) the pristine TiO$_2$ nanoparticles, (b) the TiO$_2$/Ag binary heterostructure showing evenly distributed 1-2 nm size Ag metallic nanoclusters (darker spots) on top of the larger anatase particles, (c) the (TiO$_2$-Ag)/NiFe$_2$O$_4$ (TAN) ternary heterostructure with Ag and NiFe$_2$O$_4$ nanoparticles distinguishable; the images (d-f) show the STEM micrographs for TiO$_2$, TiO$_2$/Ag and (TiO$_2$-Ag)/NiFe$_2$O$_4$ samples, respectively; (g) visualises the step-by-step growth schematics during the binary and the ternary heterostructure formation: the large red sphere represents an anatase nanoparticle, the blue and green smaller spheres the Ag and the NiFe$_2$O$_4$ smaller size nanoparticles, respectively); (h) the EDX from select areas on the (TiO$_2$-Ag)/NiFe$_2$O$_4$ sample showing the presence of the expected elements at select locations.

The nanostructures of the principal samples are depicted at a higher spatial resolution using TEM and STEM in Figure 4. The darker areas corresponding to the on average approximately 2 nm diameter Ag nanoparticles in sample TA are seen in TEM (Figure 4 b) to have a rather even distribution over the (larger, ca 20 nm diameter) TiO$_2$ nanoparticle surface (STEM, Figure 4 e). In the STEM images of the ternary TiO$_2$-Ag/NiFe$_2$O$_4$ heterostructure, the regular dark spots corresponding to Ag (metallic) nanoparticles remain visible, while the overall average size of the nanostructures apparently increases and the termination becomes somewhat less contrasted, which we ascribe to an influence of the deposition of ferrite nanocluster agglomerates from the precipitate. The size of co-precipitated NiFe$_2$O$_4$ nanoparticles can be estimated to be quite similar in size to the Ag nanoclusters, in agreement with the size estimate (above) from the Rietveld analysis. It can be seen from TEM and STEM images also that the silver resides on the anatase nanoparticles even after ferrite co-precipitation. The schematics of the build-up of the obtained two and three-component heterostructures as deduced from the TEM images is shown in Figure 4 (g). Successful Ag photodeposition and NiFe$_2$O$_4$ co-precipitation was confirmed by the EDX spectra measured at different locations within the TEM images of the ternary TiO$_2$-Ag/NiFe$_2$O$_4$ heterostructure. Particles exhibiting strong (and mutually exclusive) signals of Ag, Ni and Fe, or Ti, as displayed in Figure 4 (h).
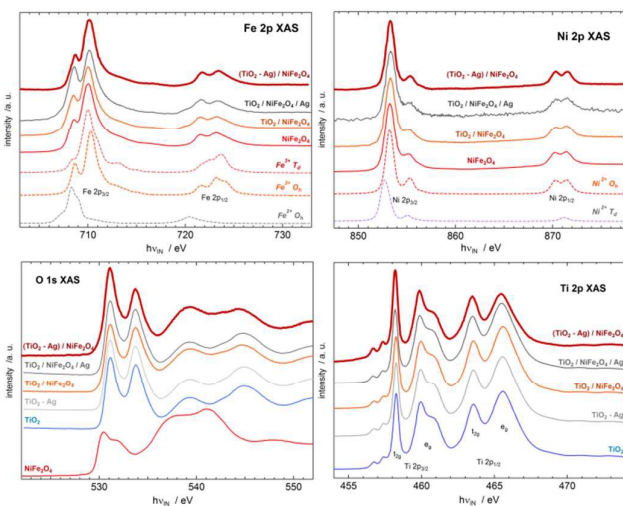

Fig. 5 The X-ray absorption spectra at the 3d transition metal 2p and the O 1s thresholds. The Fe 2p and the Ni 2p panels are complemented with simulated spectra for the particular ligand symmetries (and charge state, for Fe 2p), obtained using the CTM4XAS software[36] with crystal field parameter 10Dq values 1.6 eV (Ni^{2+} O$_h$), -1.1 eV (Ni^{2+} T$_d$), 1.4 eV (Fe^{3+} O$_h$), -0.8 eV (Fe^{3+} T$_d$) and 0.6 eV (Fe^{2+} O$_h$). (Charge transfer effects have been neglected).

XAS (Figure 5) and XPS measurements (Figure 6) at Ti 2p, Fe 2p, Ni 2p, O 1s and Ag 3d core level thresholds were carried out in order to obtain more detailed information about the chemical composition of the synthesised samples. For the 3d transition metals, the spectral shape of the near-edge XAS at the 2p absorption edges stems from the manifold of allowed 2p-3d atomic multiplet transitions, which is determined by the occupancy of the partially filled 3d states, and therefore relates directly to the charge state of the particular transition metal cation. The atomic multiplet scheme is further influenced by the (ligand) crystal field symmetry and strength in a straightforward manner, the former removing degeneracy from the 3d final states, which can result in additional allowed transitions while the latter will be proportional to energy differences between the corresponding peaks (with the transitions to the 3d levels pointed at ligands appearing at higher excitation photon energy), summarily resulting in a local probe of crystal structure and (cation) charge state. Because of hybridisation with ligand states, even the O 1s XAS shows related structures near threshold. Similar information underlies the 3d TM 2p XPS, although here the final state is (additionally) charged, which tends to smear out the spectral structure. On the other hand, the XPS chemical binding energy shifts relate to the charge state in a more linear manner, and further, the information depths of XPS and XAS differ, which makes information obtained using these techniques complementary to each other (the probe depth of XPS is determined by the inelastic scattering mean free path of the order of some a few nanometers for the electron kinetic energies used here, while XAS probe depth when carried out in the total electron yield (TEY) mode detecting all electrons irrespective of their kinetic energy is determined by electron escape depth, which can be estimated to be several tens of nanometers). However, considering the size estimates of the component nanoparticles in this study (from TEM and XRD data above), the XPS probe depth is comparable to both the silver and the nickel ferrite particles, and the XPS can be here regarded to be surface specific mainly when the larger anatase nanoparticles are considered.

The Ti 2p XAS is typical of anatase[32,33] and shows no significant differences between the samples. Similarly, the O 1s XAS remains similar to the corresponding anatase spectrum,[32] with minor relative intensity rise for the 531 eV narrow and the 539 eV broad features in the ferrite containing samples as a NiFe2O4 contribution to the spectrum.

The Ni 2p XAS of the TAN sample aligns in detail with previous experimental reports[34,35] and corresponds to Ni^{2+} in octahedral (O$_h$) coordination (as expected for NiFe$_2$O$_4$), as

exemplified by comparison with the simulated curves for the tetrahedral (T_d) and O_h ligand symmetries at the bottom of the panel, obtained using the CTM4XAS crystal field multiplet simulation software package.[36] The TAN spectrum is almost perfectly reproduced by a Ni^{2+} O_h crystal field multiplet curve for a somewhat high crystal field splitting value of 10Dq=1.6 eV (as compared to the considerations laid out in Refs. [37] and [38]); however the experimental intensity ratio of the Ni $2p_{1/2}$ peaks appears to be reproduced at similar values even in an earlier report.[38] For the other samples, the curves are very similar, indicating that Ni is dominantly incorporated at sites corresponding to the stoichiometric nickel ferrite (a small contribution from T_d antisite defects as an explanation of the slight smearing out of the spectral features as compared to the TAN, however, cannot be completely ruled out for the other samples).
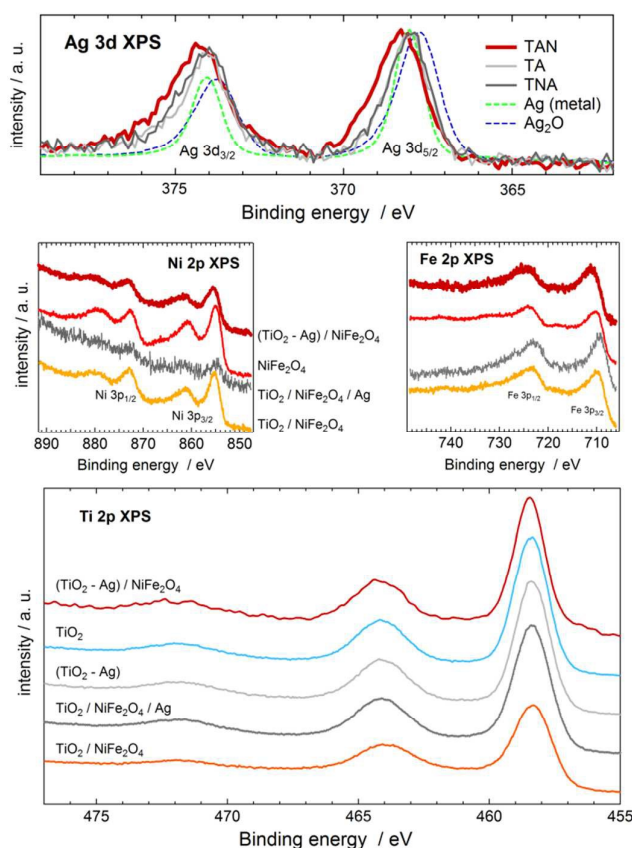

Fig. 6 The photoelectron spectra of the photocatalytic nanoheterostructures and the reference samples (as labelled) of the Ag 3d (top panel), Ni 2p (middle left), Fe 2p (middle right) and the Ti 2p core levels.

The Fe 2p XAS of the TAN sample readily reproduces the sum of the simulated curves of O_h and T_d site Fe^{3+} in O_h coordination (as expected for $NiFe_2O_4$), as exemplified by comparison with the simulated curves at the bottom of the panel. For the TNA sample, however, the Fe 2p XAS shows that the reversed synthesis steps clearly result in ample amounts of ferrous iron, which might be expected in view of the relatively

aggressive environment during silver photodeposition to which the nickel ferrite in the TNA (but not in the TAN or TN) sample is subjected. It might be of some interest then that an almost comparable amount of ferrous iron also in the TN sample, as indicated by the extra intensity of the 708 eV peak in the $2p_{3/2}$ region and significant intensity at 720 eV (below the onset of the ferric iron features in the $2p_{1/2}$ region). The comparison of the Fe 2p spectra appears to indicate that the presence of Ag nanoparticles does have a stabilising effect for stoichiometric nickel ferrite growth on the anatase nanoparticles, and that the improved functionality might be the result of the influence of the Ag particles on the synthesis.

The 3d TM 2p level XPS supports the assignments based on the corresponding XAS data, while the Fe 2p XPS of the TAN sample indicates Fe^{3+} charge state and agrees with previous reports,[34,36,39] the TNA (and to a lesser extent, the TN) peaks are shifted to lower energies with respect to the rest of the samples, indicating sizable Fe^{2+} content. The Ni 2p XPS indicates decreased Ni content in the TNA sample, while the spectra of the other samples closely resemble previously reported (both bulk and nanoparticle) $NiFe_2O_4$ Ni 2p XPS data[31,35,40] and indicate Ni^{2+} dominantly takes the Oh sites.[39]

The Ti 2p XPS remains significantly unchanged, with the Ti $2p_{3/2}$ (at 458.3 eV) and the Ti $2p_{1/2}$ (at 464.1 eV) component peaks, with the binding energies corresponding to Ti^{4+},[39] with no Ti^{3+} impurities in any of the samples, indicating that the anatase nanoparticles are not modified even at the surface by the (potentially aggressive environments) during the chemical steps of the synthesis of the binary or ternary nanoheterostructures.

Because the Ag chemical state information cannot be obtained from XAS in a similar manner to the 3d TM, the Ag 3d XPS was additionally referenced to the measured spectra of metallic and oxidised (Ag_2O) Ag 3d XPS. Notably, and at variation compared to most oxides, the Ag 3d binding energy decreases (rather than increases) by 0.4 eV, as seen in the Figure 6 (top panel) and in agreement with previous reports,[41,42] where it is also seen that the Ag 3d XPS peak of the Ag nanoparticles appears shifted relative to the oxide peak, and coincides with the metallic silver peak for all the silver containing nanoheterostructures synthesised in this study (TA, TNA, TAN). It is also seen that the peak width of the TAN Ag 3d XPS has become larger, which can be plausibly attributed to a decreasing (mean) particle size, in line with the results of an earlier study, which specifically targeted the Ag nanoparticle size influence on the Ag 3d photoelectron spectra.[43]
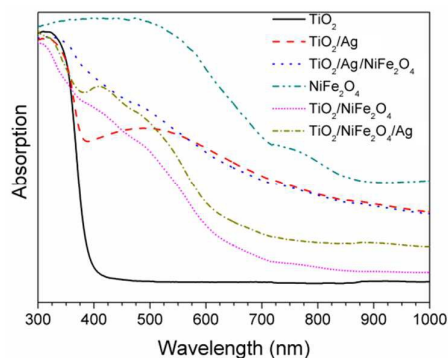
RSC Advances

Journal Name ARTICLE

Fig. 7 The measured UV-vis absorption spectra (Kubelka–Munk function) of the different photocatalyst samples.

Figure 7 gives UV-vis absorption spectra for commercial anatase TiO_2, co-precipitated $NiFe_2O_4$ and the multicomponent photocatalyst heterostructures. For TiO_2 anatase, the observed sharp absorption edge lies just below 390 nm (i. e., at the band gap value of 3.2 eV). The Ag loaded TiO_2 nanoparticles show an additional broad absorption band with an onset at approximately 1.3 eV (950 nm) and maximum at around 500 nm, attributed to a localised surface plasmon resonance (LSPR) at the Ag nanoparticles.[44] The LSPR (mean) frequency and the strength of the resonance are known to depend on nanoparticle size and shape, but also the interaction with the supporting surface (here anatase),[45,46] which can lead to the observed broad absorption. Visually, the initial white colour of commercial TiO_2 anatase nanopowder changed into greyish purple/brown after silver photodeposition. The $NiFe_2O_4$ sample exhibits broad spectrum visible light absorption similar to that observed by Harish et al.[47] and attributed there to charge transfer excitations from the O 2p dominated occupied to the Fe 3d character unoccupied valence states. An experimental band gap width value of 1.65 eV can be deduced from the optical absorption $(\alpha h\nu)^{1/2}$ versus photon energy plot, which recommends the co-precipitated $NiFe_2O_4$ as a quite efficient solar light absorber. The optical absorption of the $TiO_2/NiFe_2O_4$ sample, the TiO_2 absorption edge below 400 nm is still discernible, and below this edge the broader and lower onset energy absorption related to the ferrite. The optical absorption resembles a superposition of the spectra of the constituents, apparently containing constituent absorption thresholds and inflection points, suggesting chemically unmodified separate nanoparticles of either species.[48] Finally, the heterostructures sensitized by Ag exhibited highest light absorption over the whole measurement range for the TAN sample, whereas for the TNA sample the optical absorption onset appears to align with the ferrite rather than the (plasmonic) absorption of the silver nanoparticles.

Figure 8 shows the influence of the different photocatalysts on the optical density change of MO (with the absorption band centered at approximately 460 nm) and kinetic linear simulation curves for reaction kinetics of MO degradation by visible light irradiation using a 100 W LED light source. There was no measurable decrease in the MO solution optical density after visible light irradiation for 2 h in the absence of any photocatalyst. Only a minimal photocatalytic activity (resulting in a 2% decrease of MO optical density) was observed for the commercial anatase TiO_2 nanopowder, which can be explained as the result of the minimal spectral (tail) overlap of the light source and the TiO_2 absorption. The presence of the Ag-loaded TiO_2 nanoparticles (sample TA) gives rise to an 8% decrease of the MO concentration (corresponding to a rate constant value of $k_{TA} = 0.7 \cdot 10^{-3}$ min^{-1}). This relates to the LSPR absorption at the Ag nanoparticles in the 500-800 nm range[46,47] as seen also in the UV-visible absorption spectra in Figure 7. It has been reported previously that Ag nanoparticles on TiO_2 surface can act as light

harvesters and electron injectors into the semiconductor conduction band, as well as produce catalytic sites for ·OH formation.[47] $NiFe_2O_4$ co-precipitation on the (non-coated) TiO_2 increased the MO degradation to 18% ($k_{TN} = 1.7 \cdot 10^{-3}$ min^{-1}), which is slightly higher than the respective values for the pure co-precipitated $NiFe_2O_4$ (15%, or kN =$1.4 \cdot 10^{-3}$ min^{-1}). The small observed enhancement of photocatalytic efficiency appears to measure the role of interface charge transfer, while the slight difference of the response of the TA and the TN samples appears to agree with the estimated larger potential gradient at a $TiO_2/NiFe_2O_4$ interface, particularly in view of the broader optical absorption spectrum of silver nanoparticles on TiO_2, although it has to be kept in mind that the Ag content in the TA sample (which is optimal for the best photocatalytic activity) is smaller than the relative amount of ferrite in the $TiO_2/NiFe_2O_4$ sample.
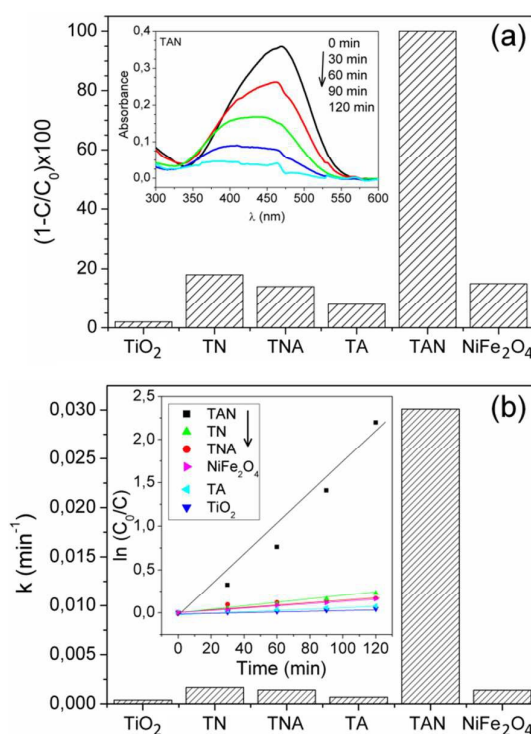

Fig. 8 (a) Relative amounts of MO photo-decomposed (as percentages of the initial amount in the solution) during 2 hours of exposure to visible light in the presence of the various photocatalyst samples; (b) Pseudo-first-order rate constants and reaction kinetics (inset) for the different photocatalysts.

A relatively quite superior visible light photocatalytic activity is seen for the TAN produced by $NiFe_2O_4$ co-precipitation in the presence of the Ag-loaded TiO_2. The miniature silver content included in the heterostructure of anatase and the ferrite produces a nearly 20-fold increase of efficiency ($k_{TAN} = 30 \cdot 10^{-3}$ min^{-1}) and leads to complete decomposition of the MO from the solution during 2 hours of visible light exposure. To exclude the effect of shape and size of the photocatalytic particles, the BET specific surface areas for different samples were studied and the pseudo-first-order

ARTICLE

Journal Name

rate constants, k values, were normalised with surface area (Table 1). The normalised k value for TAN sample was still an order of magnitude higher than for the other samples. The magnitude of the activity increase, not least as compared to the corresponding effects in the binary combinations, appears to suggest that charge separation and migration across the interfaces should favour the vectorial electron transfer of $NiFe_2O_4 \rightarrow TiO_2 \rightarrow Ag$, as shown schematically in Figure 9, similar to what has been previously observed for TiO_2-Pt/CdS heterostructures.[13] Internal electrical fields created within the heterostructure facilitate the charge separation and hence increase photochemical reactivity,[49] as the visible light absorption of the $NiFe_2O_4$ (and the plasmonic Ag nanoparticles) becomes then efficiently utilised. These charge transfer vectors can be viewed against the modest performance of the alternative ternary (TNA) sample with the silver deposited on a binary $TiO_2/NiFe_2O_4$ heterostructure, where the Ag sites will exist on both TiO_2 and $NiFe_2O_4$, possibly facilitating back transfer and recombination at a direct silver/ferrite interface. The other reason for reduced photocatalytic activity is relatively oversized Fe^{2+} content in the TNA sample (although traces of a ferrous component were also seen in the TN sample Fe 2p XAS, Figure 5) affects interface charge transfer balance, in which we have previously observed a growing ferrous content already at a much lower level to have a negative effect on photocatalytic efficiency.[50] Here the presence of Ag nanoparticles appears to have a stabilising effect in obtaining a more stoichiometric ferrite species during synthesis (the detailed mechanism of such possible stabilising effect is a matter of further investigation outside the scope of this study).
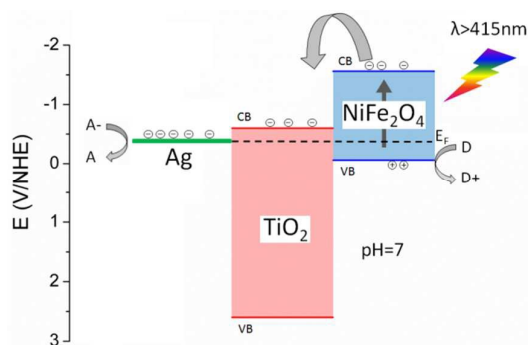

Fig. 9 Schematic representations of electron-hole separation and energy band matching of the Ag sensitized $(TiO_2$-Ag)/$NiFe_2O_4$ three-component heterostructure under visible light irradiation. The TiO_2 is not absorbing in the visible range while the smaller band gap (1.56 eV) ferrite does. Even if the Ag-sensitized anatase shows a minor photocatalytic activity due to plasmonic absorption in the silver nanoparticles, the comparison of binary and ternary nanoheterostructure photocatalytic activities (above) suggests that the role of the Ag nanoparticles in this ternary heterostructure is mainly as an electron scavenger (as indicated by the arrows), because the sum of the activities of the binary combinations (TiO_2/Ag and $TiO_2/NiFe_2O_4$) falls an

order of magnitude short of the observed activity of the ternary $(TiO_2$-Ag)/$NiFe_2O_4$ nanoheterostructure.

The ordering of the constituents and interfaces with suitable band edge gradients proves therefore to be of principal relevance in achieving high functional efficiency in the three-component $(TiO_2$-Ag)/$NiFe_2O_4$ heterostructure photocatalyst with the suppression of the electron-hole recombination rate due to effective photogenerated charge separation dependent also on the sequence of deposition.

Table 1 The surface area, pore volume, the pseudo-first-order rate constant and normalised pseudo-first-order rate constant for different photocatalysts.

Photocatalyst	Surface area S_{BET} (m^2/g)	Rate constant k (min^{-1})	Normalised rate constant k' $(g/(min·m^2)·10^3)$
TiO_2	69.52	$0.39·10^{-3}$	$0.56·10^{-2}$
$TiO_2/NiFe_2O_4$	38.07	$1.67·10^{-3}$	$4.40·10^{-2}$
$TiO_2/NiFe_2O_4/Ag$	53.35	$1.40·10^{-3}$	$2.63·10^{-2}$
TiO_2-Ag	41.39	$0.69·10^{-3}$	$1.65·10^{-2}$
TiO_2-Ag/$NiFe_2O_4$	84.15	$30.0·10^{-3}$	$35.8·10^{-2}$
$NiFe_2O_4$	83.30	$1.39·10^{-3}$	$1.67·10^{-2}$

Conclusions

We have synthesised two- and three-component visible light active photocatalysts from combinations of TiO_2, $NiFe_2O_4$ and metallic Ag nanoparticles. The visible light photocatalytic activity is strongly influenced by the choice of the compound, which is coupled to anatase TiO_2, the number of constituents included in the heterostructure and the order of deposition (of whether the ferrite or the photoreduced silver will be a 'top layer'). While silver termination in the ternary $(TiO_2/NiFe_2O_4)$/Ag structure showed some cation charge imbalance in the ferrite and a sizeable, but relatively modest efficiency (on par with the binary combinations), a large efficiency gain was observed for the $(TiO_2$-Ag)/$NiFe_2O_4$ sample obtained by $NiFe_2O_4$ co-precipitation in the presence of Ag-loaded TiO_2 nanoparticles. There the Ag sensitizer content as small as on a 1 at.% level in the $(TiO_2$-Ag)/$NiFe_2O_4$ heterostructure enhanced the rate constant for methylene orange degradation under visible light by more than an order of magnitude in comparison to the binary (not Ag-sensitized) $TiO_2/NiFe_2O_4$ heterostructure. The higher visible light photocatalytic activity in the three-component TiO_2, $NiFe_2O_4$ and Ag nanoheterostructures is attributed to an efficient separation of the visible light photogenerated charge over the interfaces via vectorial electron transfer $NiFe_2O_4 \rightarrow TiO_2 \rightarrow Ag$.

Acknowledgements

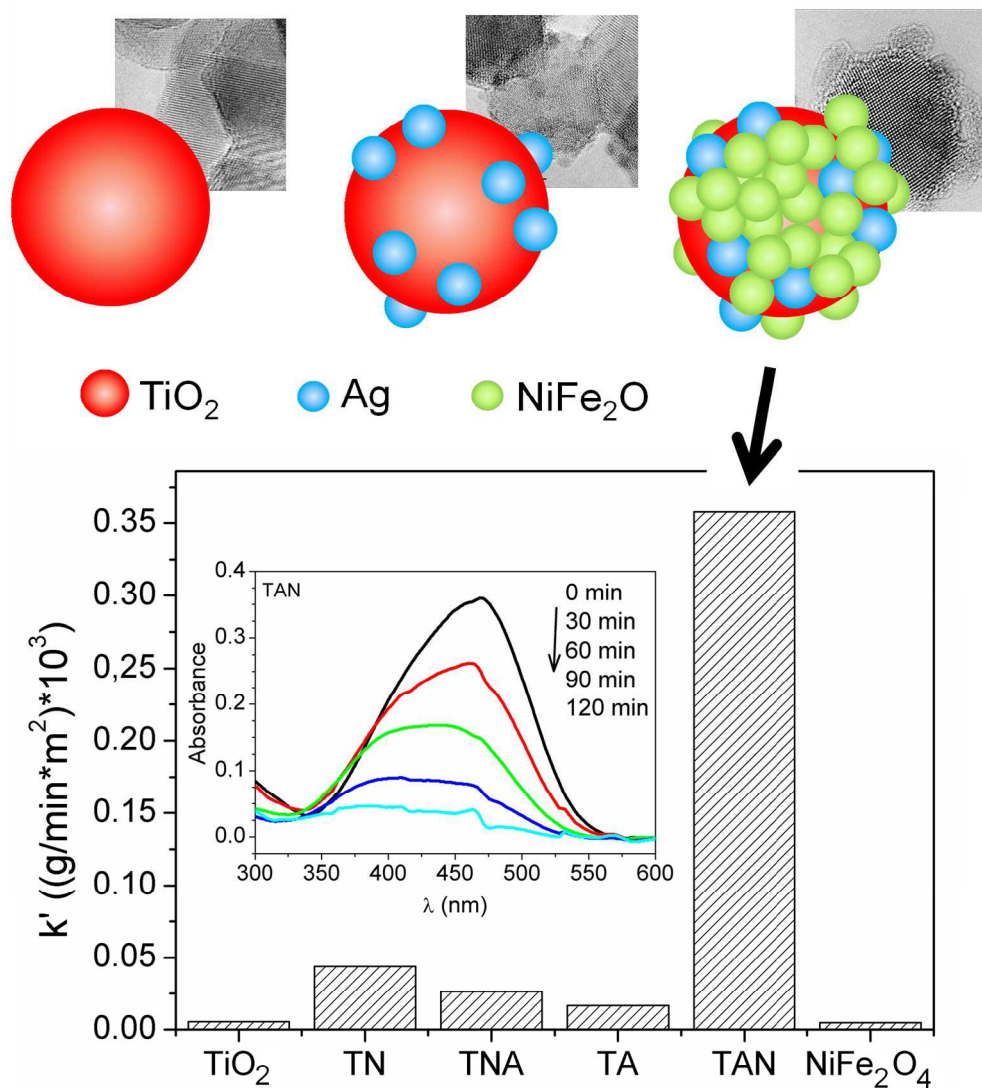**RSC Advances**

Journal Name ARTICLE

References

1   D. Robert, *Catal. Today,* 2007, **122**, 20–26.
2   J. Yan, G. Wu, N. Guan, L. Li, *Appl. Catal. B: Environ.,* 2014, **152–153**, 280–288.
3   S. Rehman, R. Ullah, A.M. Butt, N.D. Gohar, *J. Hazard. Mater.,* 2009, **170**, 560–569.
4   L. Ren, Y.-P. Zheng, D. Jiang, *Catal. Commun.,* 2009, **10**, 645–649.
5   H. Tada, T. Mitsui, T. Kiyonaga, T. Akita, K. Tanaka, *Nature Mat.*, 2006, **5**, 782–786.
6   G. Liu, L. Wang, H.G. Yang, H.-M. Cheng, G.Q. Lu, *J. Mater. Chem.*, 2010, **20**, 831–843.
7   H. Yan, J. Yang, G. Ma, G. Wu, X. Zong, Z. Lei, J. Shi, C. Li, *J. Catal.*, 2009, **266**, 165–168.
8   W. Zhou, H. Liu, J. Wang, D. Liu, G. Du, J. Cui, *ACS Appl. Mater. Interfaces*, 2010, **2**, 2385–2392.
9   H.J. Yun, H. Lee, N.D. Kim, D.M. Lee, S. Yu, J. Yi, *ACS Nano*, 2011, **5**, 4084–4090.
10 Y.-C. Chen, Y.-C. Pu, Y.-J. Hsu, *J. Phys. Chem. C*, 2012, **116**, 2967–2975.
11 P. Zhou, J. Yu, M. Jaroniec, *Adv. Mater.*, 2014, **26**, 4920–4935.
12 H. J. Yun, H. Lee, N. D. Kim, D. M. Lee, S. Yu, and J. Yi, *ACS Nano*, 2011, **5**, 4084–4090.
13 H. Park, W. Choi and M. R. Hoffmann, *J. Mater. Chem.*, 2008, **18**, 2379-2385.
14 S. Zhang, J. Li, X. Wang, Y. Huang, M. Zeng, J. Xu, *ACS Appl. Mater. Interfaces*, 2014, **6**, 22116–22125
15 S. Zhang, J. Li, X. Wang, Y. Huang, M. Zeng, J. Xu, *J. Mater. Chem. A*, 2015, **3**, 10119-10126
16 B.M. Reddy, I. Ganesh, A. Khan, *Appl. Catal. A*, 2003, **248**, 169–180.
17 R.M. Navarro, F. del Valle, J.L.G. Fierro, Int. J. *Hydrogen Energ.*, 2008, **33**, 4265-4273.
18 Y. Wang, L. Liu, L. Xu, X. Cao, X. Li, Y. Huang, C. Meng, Z. Wang and W. Zhu, *Nanoscale*, 2014, **6**, 6790-6797.
19 W. J. Zhou, Y. H. Leng, D. M. Hou, H. D. Li, L. G. Li, G. Q. Li, H. Liu and S. W. Chen, *Nanoscale*, 2014, **6**, 4698-4704.
20 S. Rtimi, R. Sanjines, C. Pulgarin, A. Houas, J.C. Lavanchy, J. Kiwi, *J. Hazard. Mater.*, 2013, **260**, 860–868.
21 A. Šutka, M. Millers, N. Döbelin, R. Pärna, M. Vanags, M. Maiorov, J. Kleperis, T. Käämbre, U. Joost, E. Nõmmiste, V. Kisand, Maris Knite, *Phys. Status Solidi A*, 2015, **212**, 796–803.
22 M. Meinert and G. Reiss, *J. Phys.: Condens. Matter*, 2014, **26**, 115503.
23 Q. - C. Sun, H. Sims, D. Mazumdar, J. X. Ma, B. S. Holinsworth, K. R. O'Neal, G. Kim, W. H. Butler, A. Gupta, and J. L. Musfeldt, *Phys. Rev. B,* 2012, **86**, 205106.
24 G. Rekhila, Y. Bessekhouad, M. Trari, *Int. J. Hydrogen Energ.*, 2013, **38**, 6335–6343.
25 A. Fujishima, X. Zhang , D. A. Trykc, Surf. Sci. Rep., 2008, **63**, 515–582.
26 A. Šutka, R. Pärna, T. Käämbre, V. Kisand, *Phys. B Condens. Matter*, 2015, **456**, 232–236.
27 L. G. Devi, K. M. Reddy, *Appl. Surf. Sci.*, 2011, **257**, 6821–6828.
28 Z.M. Khoshhesab, Reflectance IR Spectroscopy, Ch. 11 in: Infrared Spectroscopy – Materials Science, Engineering and Technology, Th. Theophanides (Ed.), InTech 2012, pp. 233-244.
29 G.E. McGuire, G.K. Schweitzer, T.A. Carlson, *Inorg. Chem.*, 1973, **12**, 2450–2453.
30 S. Zhang, J. Li, M. Zeng, J. Li, J. Xu, X. Wang, *Chem. Eur. J.* 2014, **20**, 9805–9812.
31 Michael Hoppe, Sven Döring, Mihaela Gorgoi, Stefan Cramm, and Martina Müller, *Phys. Rev. B,* 2015, **91**, 054418.
32 G. van der Laan, *Phys. Rev. B*, 1990, **41**, 12366.
33 R. Ruus, A. Kikas, A. Saar, A. Ausmees, E. Nõmmiste, J. Aarid, A. Aidla, T. Uustare, I. Martinson, *Solid State Comm.*, 1997, **104**, 199–203.
34 S. Zhou, K. Potzger, Q. Xu, K. Kuepper, G. Talut, D. Markó, A. Mücklich, M. Helm, J. Fassbender, E. Arenholz, H. Schmidt, *Phys. Rev. B*, 2009, **80**, 094409.
35 C. Klewe, M. Meinert, A. Boehnke, K. Kuepper, E. Arenholz, A. Gupta, J.-M. Schmalhorst, T. Kuschel, G. Reiss, *J. Appl. Phys.*, 2014, **115**, 123903.
36 E. Stavitski, F.M.F. de Groot, *Micron*, 2010, **41**, 687-694.
37 S. Rossano , Ch. Brouder, M. Alouani, M.-A. Arrio, *Phys. Chem. Miner.*, 2000, **27**, 170-178.
38 G. van der Laan, C. M. B. Henderson, R. A. D. Pattrick, S. S. Dhesi, P. F. Schofield, E. Dudzik, and D. J. Vaughan, *Phys. Rev. B*, 1999, **59**, 4314.
39 G. Hassnain Jaffari, A. K. Rumaiz, J. C. Woicik, and S. Ismat Shah, *J. Appl. Phys.*, 2012, **111**, 093906.
40 S. Hashimoto, A. Tanaka, *Surf. Interf. Anal.*, 2002, **34**, 262–265.
41 I.M. Arabatzis, T. Stergiopoulos, M.C. Bernard, D. Labou, S.G. Neophytides, P. Falaras, *Appl. Catal. B Environ.*, 2003, **42**, 187–201.
42 C.D. Wagner, W.M. Riggs, L.E. Davis, J.F. Moulder, Handbook of X-Ray Photoelectron Spectroscopy, Perkin-Elmer Corp., Physical Electronics Division, Eden Prairie, MN, 1979.
43 I. Lopez-Salido, D. Chan Lim, Y. Dok Kim, *Surf. Sci.*, 2005, 588, 6–18.
44 I. Tunc, M. Bruns, H. Gliemann, M. Grunze, P. Koelsch, *Surf. Interf. Anal.*, 2010, **42**, 835–841.
45 P.K. Jain, X. Huang, I. El-Sayed, M. El-Sayed, *Acc. Chem. Res.*, 2008, **41**, 1578-1586.
46 J.M. Luther, P.K. Jain, T. Ewers, A.P. Alivisatos, Nature Mater., 2011, **10**, 361–366.
47 K.N. Harish, H.S. Bhojya Naik, P.N. Prashanth Kumar, R. Viswanath, *ACS Sustainable Chem. Eng.*, 2013, **1**, 1143–1153.
48 S. Shen, L. Guo, X. Chen, F. Ren, C.X. Kronawitter, S.S. Mao, *Int. J. Green Nanotech.*, 2010, **1**, M94–M104.
49 L. Li, P. A. Salvador, G. S. Rohrer, *Nanoscale*, 2014, **6**, 24-42.
50 A. Šutka, R. Pärna, J. Kleperis, T. Käämbre, I. Pavlovska, V. Korsaks, K. Malnieks, L. Grinberga, V. Kisand, *Phys. Scr.*, 2014, **89**, 044011..

463x503mm (96 x 96 DPI)